Biosensors and Bioelectronics 189 (2021) 113367

Contents lists available at ScienceDirect

Biosensors and Bioelectronics

journal homepage: www.elsevier.com/locate/bios

Enhanced electrochemiluminescence ratiometric cytosensing based on surface plasmon resonance of Au nanoparticles and nanosucculent films

Hong Zhou [a,*], Kexin Ding [a], Qiao Yu [b], Haiyan Wang [d], Jing Liu [c,**], Zonghua Wang [b]

[a] Key Laboratory of Optic-electric Sensing and Analytical Chemistry for Life Science, Ministry of Education, College of Chemistry and Molecular Engineering, Qingdao University of Science and Technology, Qingdao, 266042, PR China
[b] Shandong Sino-Japanese Center for Collaborative Research of Carbon Nanomaterials, College of Chemistry and Chemical Engineering, Qingdao University, Qingdao, Shandong, 266071, PR China
[c] College of Chemical and Biological Engineering, Shandong University of Science and Technology, Qingdao, Shandong, 266590, PR China
[d] The Affiliated Hospital of Qingdao University, Qingdao, Shandong, 266071, PR China

ARTICLE INFO

Keywords:
Electrochemiluminescence
Ratiometric biosensor
Au nanosucculent films
Surface plasmon resonance
Au@luminol nanocomposite
CdS nanocrystals

ABSTRACT

Ramos cells are human Burkitt's lymphoma cells, which are a kind of cancer cells to facilitate the monitoring of the relevant biological processes of cancers. Sensitive and accurate detection of Ramos cells using emerging ratiometric ECL biosensing technology shows increasing importance, however, the target analytes of current ratiometric ECL biosensors are mainly limited to DNA/RNA or proteins. In this study, we proposed a dual-potential ratiometric sensing strategy for the electrochemiluminescence detection of Ramos cells based on two types of electrochemiluminescence (ECL)-responding molecular. Au nanosucculent films (AuNFs) were electrodeposited on the fluorine doped tin oxide (FTO) electrode to increase the effective area of the electrode for more efficient assembly of DNA and effectively improving the conductivity of the sensing interfaces. In the presence of Ramos cells, aptamers capped with Au@luminol would conjugate with Ramos cells and then remove from AuNFs, accompanying the decrease of ECL signal from Au@luminol. Then, Au–DNA was captured and alternately hybridized with DNA-modified CdS nanocrystals (NCs) on the surface of AuNFs with the formation of a super reticulate structure. The reticulate structure not only raised another identified ECL signal from CdS NCs but also greatly promoted its ECL intensity from the surface plasmon resonance originating from Au NPs. The value of log ($ECL_{CdS}/ECL_{luminol}$) and the logarithm of the number of cells exhibit considerable linear relation ranging from 80 to 8×10^5 cells mL^{-1} with a low detection limit of 20 cells mL^{-1} (S/N = 3). The selectivity and specificity of this dual-potential ECL sensor showed good performance and indicated considerable promise in avoiding false-positive results in detection.

1. Introduction

Recently, various techniques have been developed for the accurate detection of tumor biomarkers in the early diagnosis and effective therapy of cancer, such as fluorescence measurement (Chang et al., 2019; He et al., 2018), electrochemical assay (Traynor et al., 2020; Tavallaie et al., 2018), electrochemiluminescence (ECL) (Voci et al., 2018; Zhang et al., 2017), photoelectrochemical (PEC) assay (Yang et al., 2019; Li et al., 2019), and colorimetry (Miao et al., 2020; Lee et al., 2020). Among these techniques, the ECL method exhibited great potential for DNA/RNA detection (Jie et al., 2012; Zhou et al., 2020), immunoassay (Du et al., 2020), cancer cell detection (Liu et al., 2019), and environmental analysis (Kim et al., 2020) because of its relatively simple action method, low background, high sensitivity, and wide dynamic range. For example, Yuan's group synthesized nitrogen doped hydrazide conjugated carbon dots as anodic ECL luminophore to build a cytosensor for cell-secreted hydrogen peroxide. Upon this method, cancer cells could be rapidly distinguished from normal cells (Chen et al., 2020). Besides, Zhang et al. presented a negative ECL imaging method in which they used cell shield of the ECL emission and obtained important morphological characteristics of living cells during external stimulation and quantitative information on cell concentrations (Gao et al., 2020). Sojic and co-workers also provided a new ECL imaging method for Chinese hamster ovary (CHO) cells using

* Corresponding author.
** Corresponding author.
E-mail addresses: zhouhong@qust.edu.cn (H. Zhou), jingliu@sdust.edu.cn (J. Liu).

https://doi.org/10.1016/j.bios.2021.113367
Received 12 April 2021; Received in revised form 20 May 2021; Accepted 23 May 2021
Available online 1 June 2021

streptavidin-ruthenium complex labeled plasma membranes of CHO cells and TPA as a coreactant (Han et al., 2021). Despite many attractive advantages, some false negative or positive errors are still associated with ECL detection as a major problem. This has been blamed on the internal instrumental factors or external experimental environment. Ratiometric ECL approaches have attracted much attention as an emerging ECL detection method to eliminate these interferences and realize accurate detection (Huo et al., 2019). Ratiometric ECL detection strategies can be used to effectively eliminate the benefit of internal or external interferences from the self-calibration of two emissions in these methods, providing more convincing results in complex sample detection than traditional single-response ECL detection methods.

The ratiometric ECL sensing principles are of two types. Type I includes dual-potential biosensors based on two emitters with independent emitting potentials. Therefore, a pair of anodic/cathodic emitters with independent ECL response is necessary for dual-potential sensors. For example, the first ratiometric "dual-potential" ECL sensing approach was developed by Xu's group, which was used in DNA analysis on the basis of luminol-functionalized Pt NPs (Zhang et al., 2013). The subsequent works in "dual-potential" ECL ratiometric biosensors has extended the analytes from DNA/RNA to metal ions and protein (Wang et al., 2018c, 2019, 2020; Shao et al., 2018; Fang et al., 2019; Han et al., 2019; Cao et al., 2020a, 2020b; Hu et al., 2020). Type II includes dual-wavelength biosensors, wherein resonance energy transfer occurs between a matched ECL emitter donor/acceptor pair. Here, perfect energy-overlapped luminescent materials are highly important. Xu's group designed a g-C_3N_4/Ru$(bpy)_3^{2+}$ as a new material in a dual-wavelength ratiometric ECL biosensor to explore more capable donor/acceptor pairs for this type of ratiometric biosensors (Feng et al., 2016). Later studies also developed paired emitters based on g-C_3N_4/Ru$(dcbpy)_3^{2+}$ and the Ag NCs/Ru(II) complex or a pair of Au NP–luminol-layered double hydroxides and gold nanoclusters for high-performance ratiometric dual-wavelength ECL sensors(Huo et al., 2018; Ye et al., 2019; Zhou et al., 2018; Fan et al., 2020). A major limitation associated with this type is the requirement of an energy-matched high-performance donor/acceptor pair, which greatly limits the development of this type of ratiometric biosensor. Recently, bipolar-electrode ratiometric sensing strategies or internal-standard ratiometric biosensors were reported as novel ECL ratiometric approaches to realize visual analysis (Zhang et al., 2016; Wang et al., 2016, 2018a; Lu et al., 2018) or stable and accurate detection (Lv et al., 2018; Wang et al., 2018b; Ding et al., 2019).

Apart from accuracy, sensitivity is another important parameter for specific biomarker detection in clinical samples, wherein the analyte is at ultralow concentration. As an amplification strategy, nanomaterials have been recognized as excellent electrode materials as emitters or recognition elements in ECL biosensors (Chen et al., 2017). Additionally, nanomaterials with specific functions can provide some synergic effects to improve signal transduction and realize amplified recognition signal. Until now, many types of nanomaterials, including graphene nanomaterials, carbon nanomaterials, metal nanomaterials, and semiconductor nanocrystals (known as quantum dots, QDs), have been studied to realize ECL signal amplification (Li et al., 2017). For example, our previous study observed that the ECL signal from CdS QDs could be quenched by proximal gold nanoparticles because of Förster energy transfer. At the same time, an enhanced ECL signal was observed at a regulated distance between two nanoparticles with the ECL-excited surface plasmon resonance energy transfer from Au NPs to CdS QDs (Zhou et al., 2011a, 2011b, 2016). This distance-dependent signal amplification exhibited controlled distance between donor and acceptor, providing an extremely sensitive and smart approach for ECL analysis.

Even though the ratiometric ECL sensing methods rapidly developed, the wide application of ratiometric ECL biosensors exhibits two limits. One limit is the narrow applicability of the analytes mainly limited to DNA/RNA or proteins. New sensing strategies are urgently needed for other analytes such as cells. Furthermore, new amplification approaches are important to achieve ultrahigh sensitive detection. Based on these two limits, we proposed a dual-potential ratiometric ECL biosensing system for cancer cells. We introduced two types of nanomaterials (Au@luminol nanocomposite and CdS nanocrystal) into this system that acted as two independent ECL emitters. Scheme 1 describes the principle of this dual-potential ratiometric ECL sensing method for Ramos cells. Au nanosucculent-deposited fluorine doped tin oxide (FTO) electrode served as a working electrode with increased Au effective area and electron transfer efficiency. Thiolated DNA1 attached on the electrode via the Au–S bond. With hybridization between DNA1 and DNA2-Au@luminol, Au@luminol, as an ECL emitter, generated ECL signal at positive potential in the presence of H_2O_2. After the treatment of Ramos cells, the aptamer DNA2 functionalized with Au@luminol combined with the glycoprotein on the cell surface, releasing the corresponding number of DNA1 and further connecting DNA3-Au-DNA4. With the addition of Au-DNA4 and DNA5-modified CdS, we could find increased intensity from CdS and corresponding decreased intensity from Au@luminol, both of which were related to the concentration of the target cells.

2. Experiment section

2.1. Preparation of Au nanosucculents films modified FTO electrode

FTO glass was cut into pieces (1 cm × 4 cm) following with washing by deionized water to remove tiny pieces. Subsequently, all of them was immersed in boiling 2-propanol containing 2 M KOH for 20 min and washed with ethanol accompanying with ultrasonic concussion. After washing with water and drying at 60 °C, FTO pieces were wrapped with tape reserving a circular hole to deposited Au NFs films. FTO chips were immerged into 5.0 mL electrolyte composing of phosphate buffer (0.05 M, pH = 2), 0.054 M KCl and 5 mM $HAuCl_4$. Au nanosucculents growth on the surface of FTO under cyclic voltammetry (the potential was set from −0.8 to 0.3 V vs SCE for 50 cycles at a scan rate of 0.1 V^{-1}) and N_2 atmosphere at 60 °C. The phenomenon that the colorless glass transforms into gold indicates Au NFs was deposited on FTO successfully.

2.2. Preparation of Au-DNA4 and DNA3-Au-DNA4

The disulfide bond breaking DNA3 (1 μM) and DNA4 (10 μM) were injected in 1 mL of spheroidal Au (30 nm) at the proper proportion and incubated in room temperature for 12 h. After the aging process with 0.5 M NaCl for 10 h, the excess reagents were removed via centrifugation, and the prepared DNA3-Au-DNA4 solution was dispersed in 10 mM PBS buffer (pH = 7.4, 0.1 M NaCl) at 4 °C for further experiment. Process of synthesis of Au-DNA4 was same as that of DNA3-Au-DNA4.

2.3. Cell culture

Ramos cells were incubated in the solution composed of DMEM, 10% fetal bovine serum and 1% streptomycin and penicillin and cultured at 37 °C with 5% CO_2 and 95% air. Cells in the exponential phase of growth were collected and washed twice with ice-cold sterile PBS buffer before use.

2.4. Fabrication of work electrode and ECL detection

30 μL DNA1(10 μM) was dropped on the surface of FTO/AuNFs and kept static overnight at 4 °C. After washing with PBS buffer, MCH (1 mM) was used to block the others active site. The electrode was immersed in PBS buffer for 2 min and casted by 30 μL aptamer DNA2-Au@luminol at 37 °C for 1 h. The electrode was further incubated with different concentrations of Ramos cells, leading to the remove of aptamer DNA2-Au@luminol. 10 μL DNA3-Au-DNA4 was added on the treated electrode at 37 °C for 1 h. Finally, 30 μL DNA4-Au and DNA5-

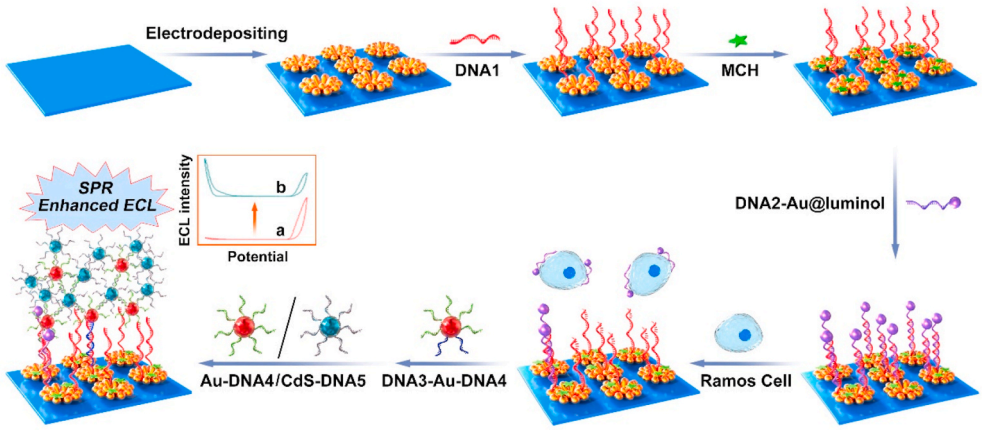

Scheme 1. Schematic presentation of assembly procedure and principle of the dual-potential cell sensor protocol.

CdS were mixed to hybrid on above FTO. The ECL detection of Ramos cells was performed under cyclic voltammetry ranging from −1.3 to 0.6 V at a speed of 0.1 V s^{-1} in 5 mL PBS buffer (0.01 M, pH 7.4, 18 mM H_2O_2).

3. Result and discussion

3.1. Sensing mechanism

Scheme 1 presents a dual-potential cell sensor protocol. First, FTO, as a conductive glass, was functionalized with the Au nanosucculent films (ANFS) through electrochemical deposition to provide a substrate for the assembly of DNA1 via the Au–S bond. After the treatment of MCH, aptamer DNA2-functionalized Au@luminol was fixed on the electrode

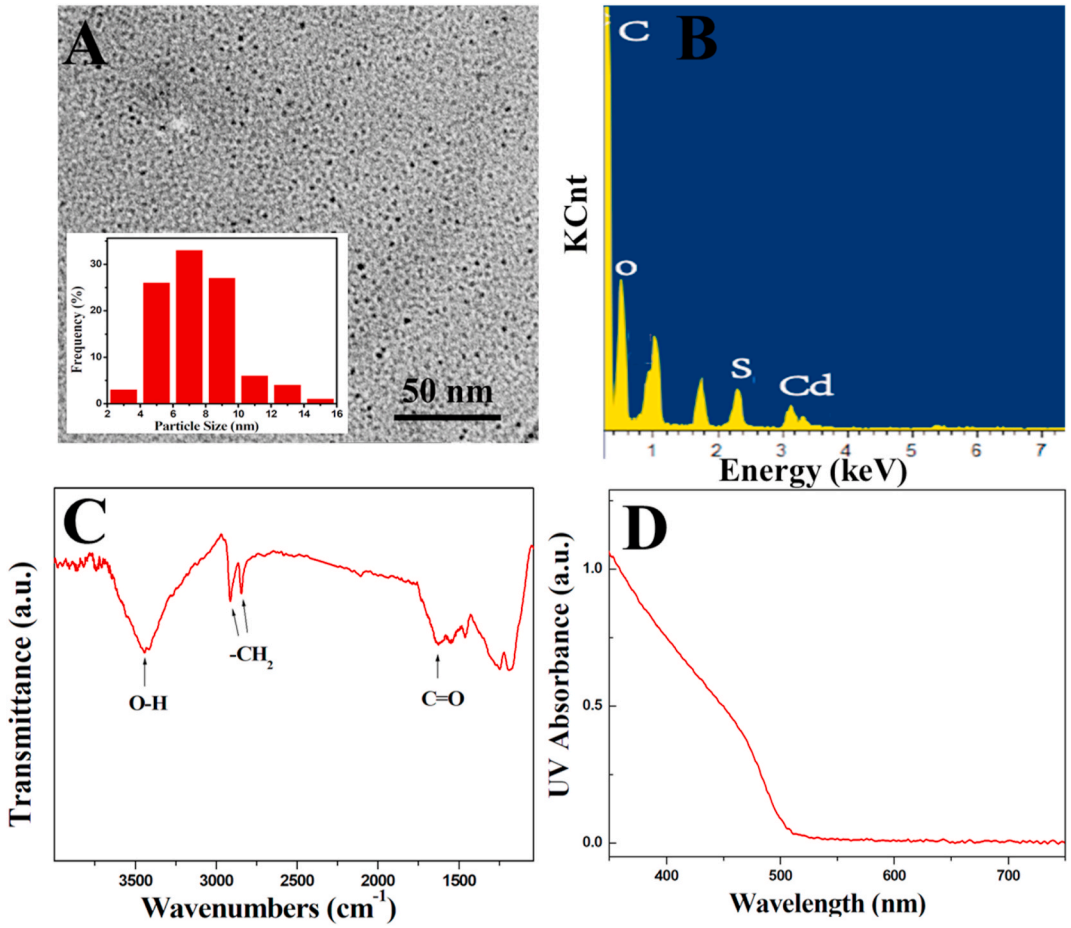

Fig. 1. (A) TEM image (insert of A: size distribution of the CdSNCs determined from TEM), (B) the SAEDX analysis, (C) FT-IR spectra, and (D) UV–vis absorption spectra of the CdSNCs.

because of the partially complementary nature of the sequence of DNA1 and DNA2, resulting in singular and intensive ECL signals at positive potential under the presence of coreactant H_2O_2. In the presence of Ramos cells, the aptamer DNA2-functionalized Au@luminol would separate from FTO because the bonding strength between the aptamer (in DNA2) and cells is stronger than that between DNA1 and aptamer (in DNA2). This results in the decrease of the luminol-generating ECL and the exposure of DNA1, based on which DNA3–Au–DNA4 could be captured. Finally, Au-DNA4 and CdS-DNA5 were added into the system. Then, the reticulate structure was obtained for the hybridization of DNA4 and DNA5, accompanying the new enhancement of ECL signal from CdS at negative potentials owing to the SPR effect of Au.

3.2. Characterization of modification

TEM images in Fig. 1A showed that the quasi-spherical shaped CdS NCs were homogeneously distributed and the size is approximately 5–8 nm. Fig. 1B showed the result of selected area energy dispersive X-ray analysis (SAEDX) of CdS NCs. The presence of C, O, S and Cd element validated the exist of CdS NCs. Fig. 1C showed the result of FT-IR spectra of mercaptoacetic acid capped CdS NCs from which we can clearly see the characteristic peaks of the functional carboxylate groups (1701 cm^{-1} asymmetric stretching vibration of C═O, 3416 cm^{-1} symmetric stretching vibration of the O–H bond), as well as the characteristic peaks of methylene (2958 cm^{-1} asymmetric stretching vibration, 2903 cm^{-1} symmetric stretching vibration). Here, due to the covalent bonds between thiols and metal atoms of the CdS NCs, no obvious characteristic peak of thiol of mercaptoacetic acid exists at 2550-2680 cm^{-1} (Chen et al., 2018). The UV–vis absorption of CdS NCs was centered at ca. 450 (Fig. 1D).

Fig. 2A displays the transmission electron microscopy (TEM) image of the as-prepared Au@luminol. The size of the resulting particles ranges from 8 to 12 nm. The UV–vis spectra (Fig. 2B) were used to characterize the synthesis of Au@luminol. Luminol showed two characterization peaks (curve b) at 300 and 360 nm. Compared with the spectrum of luminol, Au–luminol exhibited a new absorption peak at 525 nm (curve a) that was assigned to Au NPs. This indicated the formation of luminol-modified AuNPs.

In this study, FTO chips were fabricated with AuNFs using $HAuCl_4$ via electrodeposition to provide a contact point for DNA. From the SEM images (Fig. 3A), we found that the surface of Au NF film contained a stacked string of oval Au NFs. A high-magnification SEM image showed the detail morphology of the film, which was similar to a succulent plant. To further verify the successful deposition of gold, cyclic voltammetric of Au NFs deposited FTO after 50 cycles was recorded in 0.5 M H_2SO_4 solution. As shown in Fig. 3B, in the potential region from 0 V to 1.6 V, there is no observable Faradaic current for bare FTO electrode. While, for Au NFs deposited FTO electrode, there was an obvious cathodic peak at 0.88 V (vs. SCE), corresponding to the electrochemical reduction of gold oxide in the positive scan, which indicated that the surface of FTO had been covered by Au NF. The as-prepared rough gold nanostructures possessed higher active surface area and higher capture efficiency than the smooth nanostructures (Su et al., 2016). Fig. S1 presents the representative atomic force microscope (AFM) images of bare FTO (A) and Au NFs deposited FTO (B). Marked difference in the morphology and height was observed between bare FTO and Au NFs deposited FTO. Inset of Fig. S1A and B showed that the height of Au NFs/FTO increased obviously compared to the bare FTO. The results further revealed that Au NFs were successful deposited onto the surface of FTO.

The ECL response of work electrodes was detected to demonstrate the feasibility of this strategy. As can be seen from Fig. S2 A, the ECL signal in curve a (FTO/Au/DNA1) could be barely observed because the ECL-responding molecular has not been introduced on the electrode. This also indicates that the influence of the environment on this sensing system is negligible and our strategy has low background. An intensive ECL signal in curve b was detected at 0.45 V when DNA2 on Au@luminol formed a hybrid with DNA1. Curve c exhibits ignorable intensity change at 0.45 V from luminol and a weak ECL signal at −1.25 V, which may be attributed to the nonspecific adsorption of the reticulate structure generated by DNA4-Au and DNA5-CdS in the absence of Ramos cells. Along with the apparent decrease in intensity at 0.45 V, a high peak can be observed in the presence of Ramos cells, as depicted by curve d in Fig. S2A. The corresponding ECL response–potential curves of curves b and d in Fig. S2A were shown in Fig. S2B. The imparity between curves c and d demonstrate that the DNA1 in FTO would be single stranded after dipping in the cell solution because of specific binding between the cells and aptamer sequence (in DNA2). The single-stranded DNA1 could form a hybrid with DNA3–Au–DNA4 and trigger a reaction to introduce CdS in accordance with our assumption.

3.3. ECL enhancement mechanism

To further investigate the ECL enhancement of CdS NCs benefit from localized surface plasmon resonance (LSPR) effect of Au NPs, we studied the emission spectrum of CdS NCs and UV–vis absorption spectrum of Au NPs-DNA to see if the emission spectrum of the donor could perfectly match the absorption spectrum of the acceptor. The results from Fig. 4A showed that the ECL emission peak from CdS NCs at 510 nm (red curve) is well overlapped with the plasmon absorption band of Au NPs-DNA centered at 519 nm (black curve). This suggests that the two materials are a feasible LSPR-ECL couple. It could be concluded that the LSPR of Au NPs was first excited with the enhanced electromagnetic near-field which coupled back into the emission of CdS NCs* resulting in the SPR-ECL (Zhou et al., 2016).

To further explain the mechanism of this ECL enhancement, ECL-potential curves and cyclic voltammograms (CV) experiments were further carried out. Fig. 4B demonstrated that after the introduction of

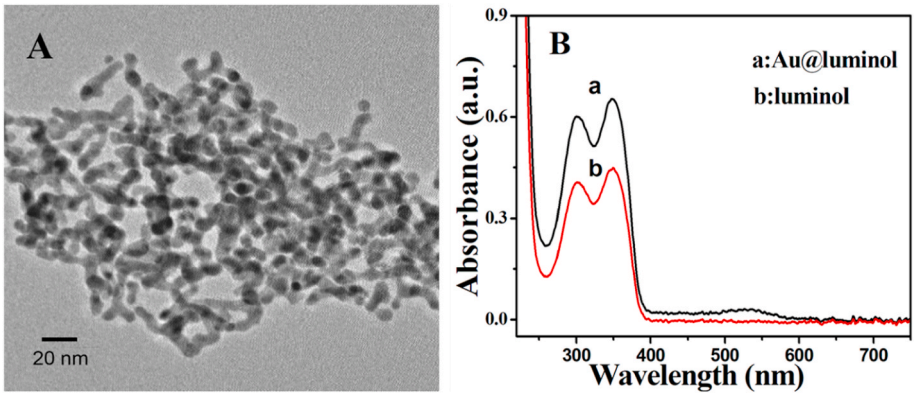

Fig. 2. (A) TEM image of Au@luminol, and (B) UV–vis absorption spectra of Au@luminol (a) and luminol (b).

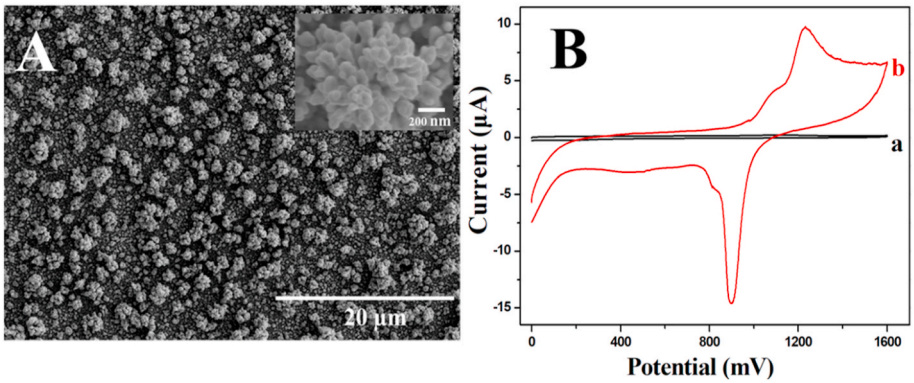

Fig. 3. (A) SEM image of the Au NFs films on FTO glass electrodeposited. The inset image is high-magnification SEM image of Au NFs; (B) Cyclic voltammograms of (a) bare FTO and (b) AuNF/FTO electrodes in 0.5 M H_2SO_4. Scan rate:100 mV s^{-1}.

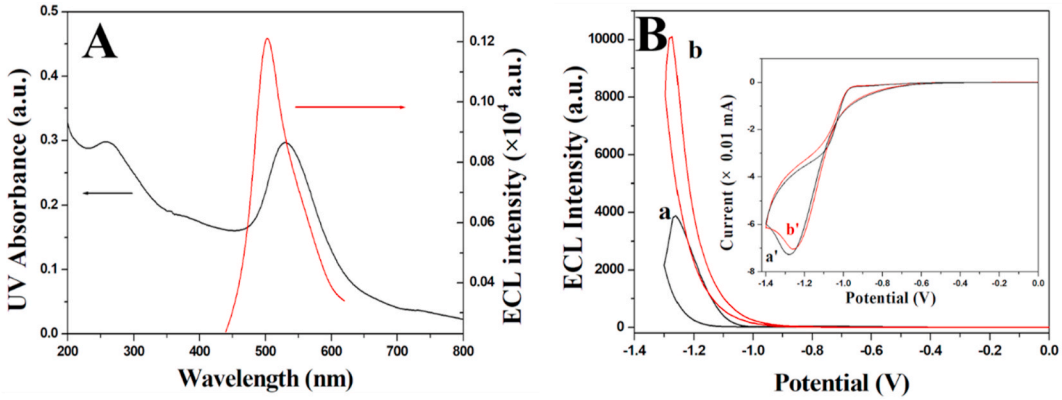

Fig. 4. (A) The UV–vis spectrum of Au NPs-DNA (black curve) and ECL spectrum of the CdS NCs (red curve); (B) ECL-potential curves and cyclic voltammograms (CV) of FTO/Au/DNA1/DNA3-CdS-DNA4/$(DNA5\text{-}CdS/DNA4\text{-}CdS)_n$ (a and a') and FTO/Au/DNA1/DNA3-Au-DNA4/$(DNA5\text{-}CdS/DNA4\text{-}Au)_n$ (b and b'). (For interpretation of the references to color in this figure legend, the reader is referred to the Web version of this article.)

Au NPs-DNA onto the electrode surface (curve b), the ECL response of CdS NCs showed a 2.5-fold enhancement. Additionally, the inset in Fig. 5B depicts a clearly shifted reduction peak of CdS NCs without (−1.3 V, curve a') or with Au NPs-DNA (−1.23 V, curve b'). This suggests that the ECL reaction becomes more effective after the assistance of Au NPs, because Au NPs could generate a strong electromagnetic field which will accelerate the excitation rate of CdS NCs (Li et al., 2016; Zhang et al., 2021). Therefore, the great enhancement of ECL is mostly benefit from the LSPR of Au NPs.

3.4. Optimization of the assay condition

Electrochemical impedance spectroscopy (EIS) was employed to present the impedance changes on the electrode during the modification process. As shown in Fig. S3, after the deposition of Au NFs on the surface of FTO upon cyclic voltammetry scanning for 30 cycles, the EIS of Au NFs/FTO (curve b) showed a lowered electron transfer compared to that of bare FTO (curve a), which was attributed to the good conductivity of Au NFs. Followed by 50 cycles, the electron transfer resistance was further decreased (curve c). The decline of semicircles proved that the presence of more Au NFs lead to further enhanced electrical conductivity. However, after the 60 cycles, Ret obvious showed an increasement (curve d) compared to that of 50 cycles. This is possibly because the portion of the Au NFs fall off from the surface of the FTO and reduces the electrical conductivity of Au NFs. Therefore, 50 cycles were chosen as the optimal condition. To achieve better ECL signal, the effects of the concentration of H_2O_2 and incubation time were investigated in this work. We studied the effect of H_2O_2 on this sensor (Fig. S4A). The ECL intensity of luminol continued to increase as the H_2O_2 concentration increased and finally reached a maximum value when the H_2O_2 concentration was 18 mM. Thus, 0.01 M PBS (pH 7.4) containing 18 mM H_2O_2 was used in ECL detection.

The ECL intensity of CdS was dependent on the amount of single-stranded DNA1, which was influenced by the concentration of target cells and the number of reticulate structures. The influence of the assembly time of Au-DNA4 and CdS-DNA5 to form the net structure was examined over the range of 15–75 min under the same conditions. As shown in Fig. S4B, the value of $ECL_{CdS}/ECL_{luminol}$ increased with the increasing time and reached the maximum value at 60 min. After the treatment of cells at same concentration, the intensity of luminol was fixed because the number of DNA2-functionalized Au@luminol separating from FTO is proportional to the amount of cells. As the reaction proceeded, increasing amount of CdS was linked, accompanied by the enhancement of CdS-generating ECL and the enlargement of the ratio of $ECL_{CdS}/ECL_{luminol}$ until balance was achieved. Based on these results, 60 min was selected for the incubation process.

3.5. Quantification detection of Ramos cells

The performance of the dual-potential cytosensor was evaluated based on the dependence between the ratio of the CdS ECL signal and luminol ECL signal in accordance with the concentration of Ramos cells. From Fig. 5A and B, we can observe that as the number of cells increased, the intensity of ECL from CdS increased, whereas that of ECL from luminol decreased. Fig. 5C shows the relation between the log $(ECL_{CdS}/ECL_{luminol})$ and concentration of cells from 0 to 8×10^5 cells

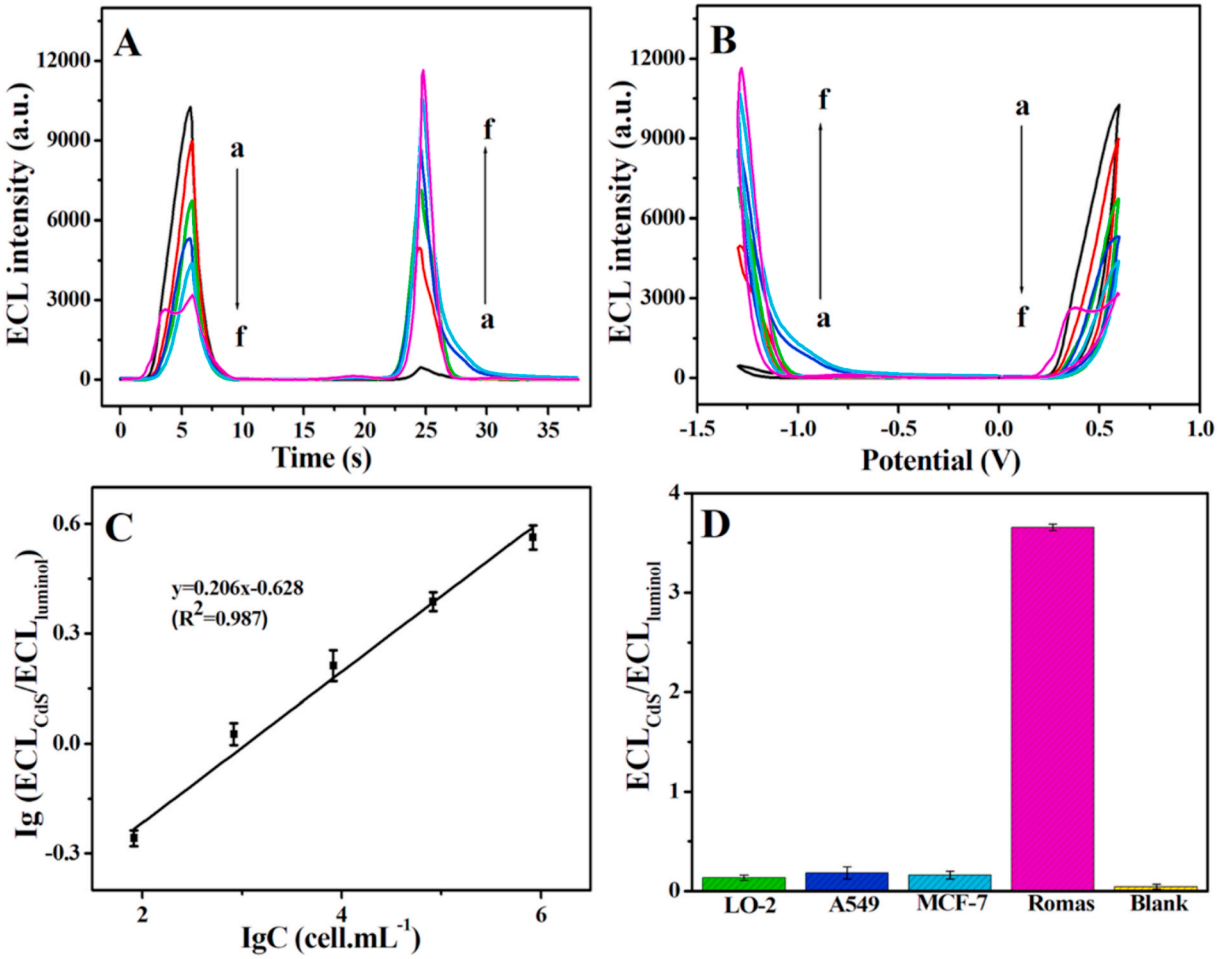

Fig. 5. (A) cyclic ECL curves of designed sensors at different concentration of cell (from a to f): 0, 80, 800, 8000, 80000,800000 cells mL^{-1}. (B) the related ECL responses of (A). (C) Relationship between the log ($ECL_{CdS}/ECL_{luminol}$) and the concentration of cell. (D) Specificity of the proposed strategy for Ramos.

mL^{-1}. Log ($ECL_{CdS}/ECL_{luminol}$) is related to the logarithm of cell concentration ranging from 80 to 8×10^5 cells mL^{-1} ($R^2 = 0.987$). The detection limit is 20 cells mL^{-1} (S/N = 3).

Selectivity and specificity are two vital factors for evaluating a newly built sensor and assay method. The LO-2 cells, A549 cells, and MCF-7 cells were selected as contrast experiments to reveal the specificity and selectivity of our project under the same operation as Ramos cells. As presented in Fig. 5D, the value of ECL_{CdS}/ECL_{lumino} exhibit tiny change compared with that of blank when several substitution cells were added into the system. In the presence of Ramos cells, the value of $ECL_{CdS}/ECL_{luminol}$ increased greatly, which can be attributed to the specific recognition between target cells and its aptamer. This indicates that this cytosensor possesses an ability to discriminate Ramos cells from other cells. The stable ECL responses under continuous potential scanning for 11 cycles were demonstrated in Fig. S5 from which we could see that this ECL-based biosensor showed promising applications with a good stability.

4. Conclusion

In this paper, a dual-potential electrochemiluminescence cytosensor was built by employing CdS NCs and Au@luminol bifunctional nanoparticles. Results demonstrate that the increase in the ECL intensity of CdS and the decrease in the ECL signal of luminol were consistent with the cell concentration. In this dual-potential sensing method, Ramos cells could be specifically identified and analyzed at a concentration as low as 20 cells mL^{-1}, which also avoids the false-positive case that usually exists in single signal sensor. We believe that other types of cancer cells can be detected via this strategy by changing the corresponding aptamer sequences in DNA. Therefore, the developed method shows wide application prospects in quantifying the target analyte.

CRediT authorship contribution statement

Hong Zhou: Conceptualization, Methodology, Funding acquisition, Writing – review & editing, Supervision. **Kexin Ding:** Data curation, Methodology, Investigation, Writing – original draft. **Qiao Yu:** Data curation, Methodology, Writing – original draft. **Haiyan Wang:** Formal analysis. **Jing Liu:** Conceptualization, Writing – review & editing. **Zonghua Wang:** Writing – review & editing.

Declaration of competing interest

The authors declare that they have no known competing financial interests or personal relationships that could have appeared to influence the work reported in this paper.

Acknowledgments

We gratefully acknowledge the support from the National Natural Science Foundation of China (Grant Nos. 21675074).

Appendix A. Supplementary data

Supplementary data to this article can be found online at https://doi.org/10.1016/j.bios.2021.113367.

References

Cao, N., Zhao, F., Zeng, B., 2020a. Sensor. Actuator. B Chem. 313, 128042.
Cao, S.P., Luo, Q.X., Li, Y.J., Liang, R.P., Qiu, J.D., 2020b. Chem. Commun. 56, 5625–5628.
Chang, X., Zhang, C., Lv, C., Sun, Y., Zhang, M., Zhao, Y., Yang, L., Han, Da, Tan, W., 2019. J. Am. Chem. Soc. 141, 12738–12743.
Chen, Y., Zhou, S., Li, L., Zhu, J.J., 2017. Nano Today 12, 98–115.
Chen, X.Q., Gui, W.Y., Ma, Q., 2018. Anal. Chim. Acta 1009, 73–80.
Chen, A., Liang, W., Wang, H., Zhuo, Y., Chai, Y., Yuan, R., 2020. Anal. Chem. 92, 1379–1385.
Ding, C., Li, Y., Wang, L., Luo, X., 2019. Anal. Chem. 91, 983–989.
Du, D., Shu, J., Guo, M., Haghighatbin, M.A., Yang, D., Bian, Z., Cui, H., 2020. Anal. Chem. 92, 14113–14121.
Fan, Z., Lin, Z., Wang, Z., Wang, J., Xie, M., Zhao, J., Zhang, K., Huang, W., 2020. ACS Appl. Mater. Interfaces 12, 11409–11418.
Fang, D., Zhang, S., Dai, H., Lin, Y., 2019. Biosens. Bioelectron. 146, 111768.
Feng, Q.M., Shen, Y.Z., Li, M.X., Zhang, Z.L., Zhao, W., Xu, J.-J., Chen, H.-Y., 2016. Anal. Chem. 88, 937–944.
Gao, H., Han, W., Qi, H., Gao, Q., Zhang, C., 2020. Anal. Chem. 92, 8278–8284.
Han, Z., Shu, J., Liang, X., Cui, H., 2019. Anal. Chem. 91, 12260–12267.
Han, D., Goudeau, B., Jiang, D., Fang, D., Sojic, N., 2021. Anal. Chem. 93, 1652–1657.
He, L., Lu, D., Liang, H., Xie, S., Zhang, X., Liu, Q., Yuan, Q., Tan, W., 2018. J. Am. Chem. Soc. 140, 258–263.
Hu, Y., He, Y., Peng, Z., Li, Y., 2020. Biosens. Bioelectron. 167, 112490.
Huo, X.-L., Zhang, N., Yang, H., Xu, J.-J., Chen, H.-Y., 2018. Anal. Chem. 90, 13723–13728.
Huo, X.-L., Lu, H.-J., Xu, J.-J., Zhou, H., Chen, H.Y., 2019. J. Mater. Chem. B 7, 6469–6475.
Jie, G., Yuan, J., Huang, T., Zhao, Y., 2012. Electroanalysis 24, 1220–1225.
Kim, T., Kim, H.J., Shin, I.S., Hong, J.I., 2020. Anal. Chem. 92, 6019–6025.
Lee, H., Lee, J., Lee, S.G., Doyle, P.S., 2020. Anal. Chem. 92, 5750–5755.
Li, M.X., Zhao, W., Qian, G.S., Feng, Q.M., 2016. Chem. Commun. 52, 14230–14233.
Li, L., Chen, Y., Zhu, J.J., 2017. Anal. Chem. 89, 358–371.
Li, P.P., Cao, Y., Mao, C.J., Jin, B.K., Zhu, J.J., 2019. Anal. Chem. 91, 1563–1570.
Liu, G., Jin, B.K., Ma, C., Chen, Z., Zhu, J.J., 2019. Anal. Chem. 91, 6363–6370.
Lu, H.J., Zhao, W., Xu, J.J., Chen, H.Y., 2018. Biosens. Bioelectron. 102, 624–630.
Lv, Y., Chen, S., Shen, Y., Ji, J., Zhou, Q., Liu, S., Zhang, Y., 2018. J. Am. Chem. Soc. 140, 2801–2804.
Miao, X., Zhu, Z., Jia, H., Lu, C., Liu, X., Mao, D., Chen, G., 2020. Actuator. B Chem. 320, 128435.
Shao, K., Wang, B., Nie, A., Ye, S., Ma, J., Li, Z., Lv, Z., Han, H., 2018. Biosens. Bioelectron. 118, 160–166.
Su, S., Wu, Y., Zhu, D., Chao, J., Liu, X., Wan, Y., Su, Y., Zuo, X., Fan, C., Wang, L., 2016. Small 12, 3794–3801.
Tavallaie, R., McCarroll, J., Le, Grand M., Ariotti, N., Schuhmann, W., Bakker, E., et al., 2018. Nat. Nanotechnol. 13, 1066–1071.
Traynor, S.M., Wang, G.A., Pandey, R., Li, F., Soleymani, L., 2020. Angew. Chem. Int. Ed. 59, 2–8.
Voci, S., Goudeau, B., Valenti, G., Lesch, A., Jovic, M., Rapino, S., Paolucci, F., Arbault, S., Sojic, N., 2018. J. Am. Chem. Soc. 140, 14753–14760.
Wang, Y., Zhao, W., Dai, P.P., Lu, H.J., Xu, J.J., Pan, J., Chen, H.-Y., 2016. Biosens. Bioelectron. 86, 683–689.
Wang, Y., Ji, S.Y., Xu, H.Y., Zhao, W., Xu, J.J., Chen, H.Y., 2018a. Anal. Chem. 90, 3570–3575.
Wang, Y., Liu, F.R., Cao, J.T., Ren, S.W., Liu, Y.M., 2018b. Biosens. Bioelectron. 102, 525–530.
Wang, Y., Shan, D., Wu, G., Wang, H., Ru, F., Zhang, X., Li, L., Qian, Y., Lu, X., 2018c. Biosens. Bioelectron. 106, 64–70.
Wang, Y., Zhang, Y., Sha, H., Xiong, X., Jia, N., 2019. ACS Appl. Mater. Interfaces 11, 36299–36306.
Wang, J., Haghighatbin, M.A., Shen, W., Mi, L., Cui, H., 2020. Anal. Chem. 92, 7062–7070.
Yang, H., Hu, M., Li, Z., Zhao, P., Xie, L., Song, X., Yu, J., 2019. Anal. Chem. 91, 14577–14585.
Ye, J., Zhu, L., Yan, M., Zhu, Q., Lu, Q., Huang, J., Cui, H., Yang, X., 2019. Anal. Chem. 91, 1524–1531.
Zhang, H., Xu, J.J., Chen, H.Y., 2013. Anal. Chem. 85, 5321–5325.
Zhang, H., Wang, Y.Z., Zhao, W., Xu, J.J., Chen, H.Y., 2016. Anal. Chem. 88, 2884–2890.
Zhang, H., Li, B., Sun, Z., Zhou, H., Zhang, S., 2017. Chem. Sci. 8, 8025–8029.
Zhang, Q., Tian, Y., Liang, Z.H., Wang, Z.Z., Xu, S.P., Ma, Q., 2021. Anal. Chem. 93, 3308–3314.
Zhou, H., Liu, J., Xu, J.J., Chen, H.Y., 2011a. Anal. Chem. 83, 8320–8328.
Zhou, H., Liu, J., Xu, J.J., Chen, H.Y., 2011b. Chem. Commun. 47, 8358–8360.
Zhou, H., Han, T., Wei, Q., Zhang, S., 2016. Anal. Chem. 88, 2976–2983.
Zhou, Y., Yu, Y., Chai, Y., Yuan, R., 2018. Talanta 181, 32–37.
Zhou, T., Huang, R., Huang, M., Shen, J., Shan, Y., Xing, D., 2020. Adv. Sci. 7, 1903661.